Quantification of the effect of multiple scattering on array imaging performance

Alexander Velichko

Abstract—A quantitative assessment of the detection limit is an important task in a range of fields, where imaging in a random scattering medium is performed. All images suffer, to varying extents, from coherent noise including speckle caused by material microstructure. The quality of images can be greatly improved by using phased arrays because of the possibility to focus backscattered signals in transmission and reception. As a consequence, under the single scattering assumption, the signal-to-noise ratio increases with frequency due to better focusing. However, in reality, material structural noise severely affects the detection performance, and especially at high frequencies and large penetration depths. The actual detection limit depends on the type of imaged target and the material properties, but the underlying physical reason is the same and is related to the increase in the contribution of multiple scattering to the measured data. Thus, in this paper a method for estimating the proportion of the multiple scattering contribution in the total image intensity is proposed. Experimental results are presented for ultrasonic array immersion imaging of a collection of randomly distributed steel rods, as well as direct contact imaging of highly scattering polycrystalline materials. It is shown that the signal-to-noise ratio (SNR) as a function of frequency and imaging depth is directly correlated with the measured single scattering rate. Moreover, the detection limit corresponds to the onset of the dominant multiple scattering regime, when the multiple scattering rate approaches 100%.

I. Introduction

Imaging and detection in a random scattering medium is a topic of significant interest in many different fields, including non-destructive testing (NDT), medical imaging, seismology, radar, underwater acoustics, etc [1]–[9]. Standard imaging methods are based on the single scattering assumption and effectively focus the scattered signals back at the scatterer location. However, single scattering is usually accompanied by multiple scattering, although the latter can be relatively small. From the imaging perspective the multiple scattering acts as a coherent noise and results in image quality degradation at high frequencies and large penetration depths.

The traditional NDT method of evaluating the limits of inspection consists of performing measurements on a large number of samples with artificial defects [10]. In order to reduce the cost of this procedure, there is a trend to use a model-based assessment instead of real testing and a number of methods have been proposed recently. For example, an analytical model for predicting the signal-to-noise ratio (SNR) on a phased array image under the single scattering assumption has been developed [1] and then applied for comparison of ultrasonic array imaging algorithms in highly scattering materials [4].

The full complexity of the multiple scattering phenomenon can only be taken into account by using numerical techniques, such as Finite Element (FE) methods. The most significant advancement has been in the utilisation of Graphics Processing Units (GPU), which have been shown to reduce the processing time by 1-2 orders of magnitude [11]. This allowed the study of elastic waves propagation within polycrystalline materials in two and three dimensions and the comparison of the numerically observed scattering against well-established analytical multiple scattering theory [12].

Relative complexity and computational cost of pure numerical approaches motivated the development of an alternative modeling technique, which combines a simulated defect response with experimentally measured structural noise [13], [14]. It has been demonstrated that this approach gives accurate results for the full range of SNRs, where meaningful data can be drawn from the image (defined as a SNR threshold of 12.5 dB above the root mean square (RMS) noise amplitude).

Note, that the assessment of the detection limit in all mentioned modelling methods was performed for some particular defect types and sizes. In addition, FE methods also require some prior knowledge of the material micro-structure (for example, grain size and distribution). However, in all cases the underlying physical reason of the detection limit is the same and corresponds to the increase of the multiple scattering contribution (when absorption loses are small). Therefore, the imaging performance can potentially be predicted based on the quantitative estimation of the multiple scattering rate. This is the main motivation for the current work.

Another application area, which can benefit from the analysis of the multiple scattered waves, is material characterisation. The sensitivity of backscattered signals to the material microstructure is well known and has been extensively used for the estimation of material properties [15], [16]. Recently a new approach to estimate the relative contribution of multiple scattering in backscattered waves was developed by Aubry et al. [6]. The method is based on the specific phase property of the single-scattering contribution to discriminate single- from multiple scattered waves. This so-called multiple scattering filter (MSF) can be used to improve detection

A. Velichko is with the Department of Mechanical Engineering, University of Bristol, Bristol, UK (e-mail: a.velichko@bristol.ac.uk).

This work was funded by the Engineering and Physical Sciences Research Council (EPSRC) grant number EP/L015587/1 through the UK Research Centre in Non-Destructive Evaluation (RCNDE).

in random scattering media [17], [18], or to characterise the weakly scattering medium (human soft tissue) [6]. This technique was also applied as a metric to compare experimental measurements and FE simulations [19], and to investigate the effect of microstructural elongation in titanium alloys [20].

However, the multiple scattering proportion in the MSF method is estimated in the raw time-domain data. On the other hand, the detection limit is defined by the image SNR, so it is important to know the relative multiple scattering rate in the image domain, rather than in the raw data. In this paper, a method for estimating the relative multiple scattering rate directly on ultrasonic array images is proposed. The crucial observation is that the single and multiple scattering contributions have a specific structure in the image domain and this property can be used to estimate their relative proportion. It is then demonstrated on experimental and modeling examples, that the estimated multiple scattering rate is directly correlated with the detection limit as a function of the imaging frequency and depth.

II. Experimental configuration

In this paper, 2-D imaging using a 1-D linear ultrasonic array is considered. The measurements were conducted in immersion and direct contact configurations. In both situations, Cartesian coordinate axes (x, z) are defined with the z axis normal to the array (see Fig. 1).

For immersion measurements, the scattering medium represents a collection of randomly placed, parallel steel rods, called a Random Rod Forest (RRF) following the paper [20]. The diameter of each rod is 0.76 mm and the density is 12 rods/cm^2. Note that multiple scattering effects in a similar random medium have been extensively studied before in [17], [20], [21]. The system is schematically illustrated in Fig. 1(a). All measurements on the RRF sample were performed using 128-element 5MHz array with parameters given in Table I. The distance between the array and the specimen was 10 mm and for all results in the following sections the distance $z = 0$ corresponds to the front edge of the RRF specimen.

In the second measurement configuration the same 5MHz 128-elements array #2 (Table I) was placed in direct contact with the testing sample as shown in Fig. 1(b). The material was copper (experimentally measured longitudinal velocity is 4690 m/s) and in this case the backscattered signals are determined by the grain boundaries scattering phenomenon. Note that the choice of the material was based on the requirement that the transition from dominant single to dominant multiple scattering occurs within the frequency range of the available array transducer.

Practically, it is difficult to find a pure single scattering material. The single scattering is always accompanied by the multiple scattering, although the latter can be relatively small. Therefore, an array response for the pure single scattering medium was simulated using a hybrid ray-tracing model [4] and the specification for the 5MHz 128-elements array #2 was used in this case. Only longitudinal waves were modelled as array elements are mostly sensitive to the longitudinal waves within the considered incident/scattered angular range of $\pm 30°$. The scattering medium is represented by a random distribution of omnidirectional point scatterers with a density of approximately 2 scatterers/λ^2, where λ is the ultrasonic wavelength at the array center frequency [4]. The host material properties were chosen to be the same as in the experimental test, and the scatterer's amplitudes were uniformly distributed as illustrated in Fig. 1(c).

In addition to experimental array measurements, a Finite Element (FE) method was also used to simulate array signals scattered by a grain structure. Pogo software package [11] was chosen as the FE solver. The Pogo has the advantage of using the computational power of graphics processing units (GPUs) and is reported to reduce the processing time by up to 200 times compared to a CPU-based commercial software. A detailed description of the modelling procedure can be found in [14]. The specimen was 40 mm deep and the material properties were chosen close to the copper specimen used in experimental measurements as $c_{11} = 168.6$GPa, $c_{12} = 121.4$GPa, $c_{44} = 75.4$GPa and $\rho = 8960$kg/m^3 (c_{11}, c_{12}, and c_{44} are elastic constants of a cubic material). The longitudinal velocity in this case is 4690 m/s. The mean grain size was 100 μm and the FMC data were modeled for the 2.5 MHz 64 elements array #1 with the parameters listed in Table I.

III. The signature of single and multiple scattering in the time-domain

A. Backscattering intensity

The array data are acquired using the Full Matrix Capture (FMC) procedure [22] and represents a dataset of transmitter-receiver signals $g_{fmc}(t, x_T, x_R)$. The variables x_T and x_R denote the coordinates of transmitter and receiver elements, respectively. Following the approach described in papers [17], [20], a short time Fourier analysis of the FMC data is performed. Firstly, the time window is used to approximately select a portion of the signals associated with the same scattering events in the medium at each depth z. Note that, strictly speaking, this is only possible if the scattering region of interest is located in the far-field of the whole array, when the travel time from array elements to the region of interest is predominantly defined by the depth z. In this paper, the scattering medium is located in the near field of the array and, strictly speaking, the time window can not be associated with the same depth for all transmitter-receiver pairs. However, there are some important effects related to the single and multiple scattering which are still observable and useful to consider in the context of the next section (where single and multiple scattering are analysed in the imaging domain).

The time traces $g_{fmc}(t, x_T, x_R)$ are truncated into temporal intervals Δt as

$$G_{fmc}(T, t, x_T, x_R) = g_{fmc}(t, x_T, x_R)W(t - T), \qquad (1)$$

TABLE I
Specification of the array transducers used in simulations and experimental measurements.

	Number of elements	Centre frequency, f_0, MHz	-6 dB Bandwidth, $\%f_0$	element dimensions, mm		
				pitch	width	length
#1	64	2.5	200	0.5	0.35	-
#2	128	5	68	0.3	0.2	15

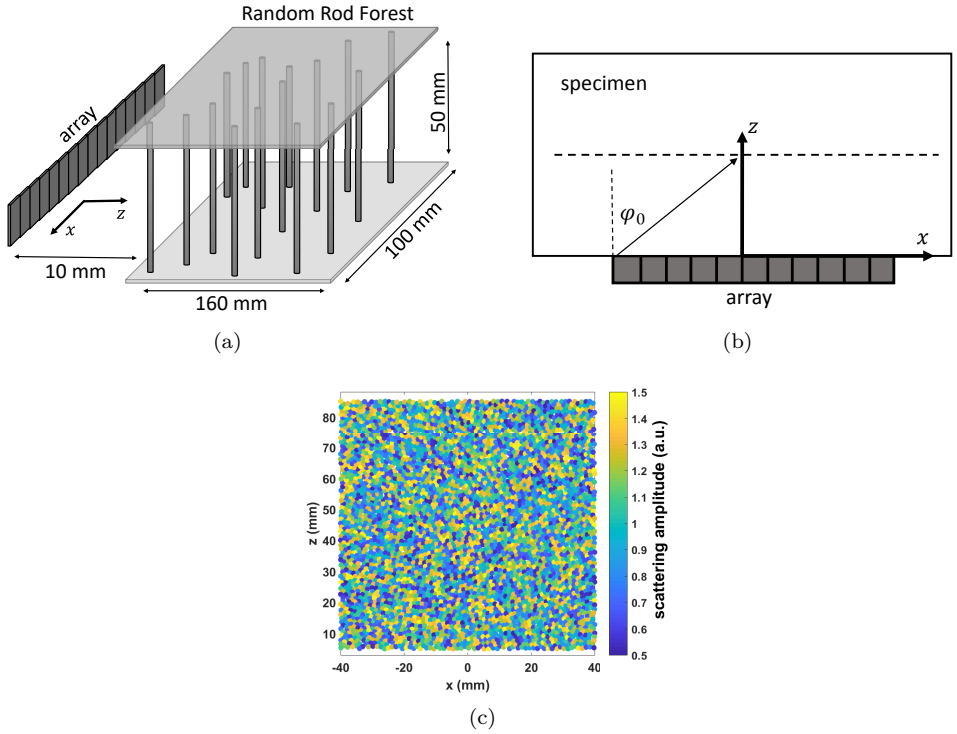

Fig. 1. Array measurement geometry for (a) the Random Rod Forest (RRF) sample (dimensions are not to scale), and (b) direct contact measurements. (c) Distribution of the point scatterers for the single scattering modelling example, color map corresponds to the scattering amplitudes.

where the window function $W(t) = 1$ for $0 \leq t \leq \Delta t$ and $W(t) = 0$ elsewhere. Then the time data $G_{fmc}(T, t, x_T, x_R)$ is transformed into the frequency, f, domain and, finally, the matrix $G_{fmc}(T, f, x_T, x_R)$ at each time T and frequency f is obtained.

The array data g_{fmc} can be represented as a sum of single and multiple scattering contributions:

$$g_{fmc} = g^S_{fmc} + g^M_{fmc}. \tag{2}$$

In order to analyse the structure of single and multiple scattering array data, the mean backscattered intensity as a function of the transmitter-receiver distance $\Delta x = |x_T - x_R|$ is considered [6], [20],

$$I(\Delta x, T, f) = \left\langle |G_{fmc}(T, f', x_T, x_R)|^2 \right\rangle_{|x_T - x_R| = \Delta x, |f' - f| \leq \Delta f}, \tag{3}$$

here the symbol $\langle \cdot \rangle$ denotes an average over the variables in the subscript, i.e. transmitter-receiver pairs with the same distance between transmitter and receiver elements, and also frequency within some interval Δf.

The behaviour of the function $I(\Delta x)$ for the purely single scattering random medium is illustrated in Fig. 2(a). Note that it is convenient to use the normalised transmitter-receiver distance $\Delta x/\lambda$, where λ is the longitudinal wavelength at the frequency f. It can be seen that the intensity in general decreases as the transmitter-receiver distance increases. This can be explained by the fact that the scattering medium is located in the near field of the array. In this case, the backscattering intensity as a function of transmitter-receiver separation is affected by the beam-spreading effect and array element directivity. However, for the relatively small distances Δx the intensity can be approximately considered to be constant.

The backscattered intensity for different random scattering media in the dominant multiple scattering regime is shown in Fig. 2(b). Similarly to the single scattering case the intensity decreases at large transmitter-receive distances because of the near field effect. However, in the vicinity of the pulse-echo point $\Delta x = 0$ a specific structure of the intensity is clearly observable. It can be seen that the intensity has a sharp peak at $\Delta x = 0$ and then drops to approximately half of its maximum value at $\Delta x > 0$. This is the so-called coherent backscattering phenomenon. It is

important to stress that the coherent backscattering effect represents a unique signature of the multiple scattering in random media, irrespective of the nature of the scattering medium or the type of waves, and was actively studied both experimentally and theoretically [5], [6], [20]. Its physical origin is briefly recalled next.

Each transmitter-receiver signal is represented by the sum of partial waves, A_p, travelled along various paths in the scattering medium. Then the intensity can be written as

$$I = \sum_p |A_p|^2 + \sum_p \sum_{q \neq p} A_p A_q^* = I_{inc} + I_{coh}, \qquad (4)$$

where asterisk sign means complex conjugate. The first term is incoherent intensity and is given by the sum of intensities associated with all possible paths. The second term is coherent intensity and depends on the phase difference between waves propagated along different paths. If scatterers are randomly located and non-correlated, then the average coherent intensity tends to zero. However, this is not true for the pulse-echo intensity at $\Delta x = 0$. In this case for any partial wave, A_p, there is a reciprocal wave, A_q, which travels along the reciprocal path and has exactly the same phase as A_p. This situation is schematically illustrated in Fig. 3. Therefore, if $\Delta x = 0$ the coherent intensity term doesn't tend to zero, and the total intensity is doubled compared to the case of different transmit and receive elements $\Delta x \neq 0$.

B. Multiple scattering estimator in the time domain

The two cases considered above (pure single and multiple scattering) represent two extremes, and in general both single and multiple scattering contributions are present in the backscattered signals. In a random scattering medium these contributions are uncorrelated, and, therefore, the total intensity can be written as a sum of single and multiple scattering intensities:

$$I = I_S + I_M. \qquad (5)$$

It is convenient to express the intensities I_S and I_M as

$$I_S(\Delta x) = a_S I_{Sn}(\Delta x), \quad I_M(\Delta x) = a_M I_{Mn}(\Delta x), \qquad (6)$$

where $a_{S,M} = \max_{\Delta x} I_{S,M}$. Based on the empirical observations performed above, the normalised intensities I_{Sn}, I_{Mn} can be written in the following form (at least for relatively small values of Δx):

$$I_{Sn}(\Delta x) = 1, \qquad (7)$$

$$I_{Mn}(\Delta x) = \begin{cases} 1, & \Delta x = 0 \\ 0.5, & \Delta x \neq 0. \end{cases} \qquad (8)$$

The final goal is to estimate the single and multiple scattering contribution as a fraction of the total intensity:

$$\delta_{S,M} = \frac{\max I_{S,M}}{\max I} = \frac{a_{S,M}}{a_S + a_M}. \qquad (9)$$

Taking into account (5), (6) and the equality $\delta_S + \delta_M = 1$, the following expression for the single and multiple scattering rates can be obtained:

$$\delta_S = 1 - \delta_M, \quad \delta_M = \frac{\langle I_n - I_{Sn} \rangle_{\Delta x}}{\langle I_{Mn} - I_{Sn} \rangle_{\Delta x}}, \qquad (10)$$

where I_n is the normalised total intensity,

$$I_n(\Delta x) = \frac{I(\Delta x)}{\max I}. \qquad (11)$$

In expression (10) an additional averaging over some interval $\Delta x_1 \leq \Delta x \leq \Delta x_2$ is performed in order to reduce measurement noise. For all examples below the values $\Delta x_1 = \lambda$ and $\Delta x_2 = 5\lambda$ were chosen. Properties (7) and (8) of the single and multiple scattering allow us to simplify expression for δ_M as

$$\delta_M = 2\,(\,1 - \langle I_n \rangle_{\Delta x}\,). \qquad (12)$$

Finally, it should be noted that because of the near-field measurement configuration the described method is not accurate, especially for small times T. However, the general approach discussed here provides the basis for the multiple scattering estimation in the image domain, considered in the next section.

IV. The signature of single and multiple scattering in the imaging domain

A. Generalised image

The array data are usually transformed into an image by some imaging algorithm. The majority of the array imaging methods are based on the single scattering assumption and effectively focus the scattered signals back to their scatterer locations. Therefore, an array image is much more sensitive to the single scattering contribution compared to the raw time-domain data. The multiple scattering contribution in this case acts as a noise, and is the main reason for the image quality degradation at high frequencies and large imaging depths. Therefore, from the imaging perspective, it is useful to estimate the multiple scattering rate associated with the image amplitude. Another advantage of considering images instead of the raw array data is that in this case it becomes possible to estimate the multiple scattering contribution as a function of imaging depth. As it was mentioned in the previous section this is difficult to achieve in the time-domain, because scattering from different depths cannot be separated in time for the near-field array measurement configuration.

In this section the approach described previously is extended to estimate the single and multiple scattering rates directly on an array image. The difficulty is that this method is based on the specific properties (signatures) of the backscattering intensity as a function of transmitter-receiver separation, and it is not straightforward how this approach can be applied to array images if a conventional 2D image is considered. The key idea is based on the concept of a reversible imaging operator [23], [24], which

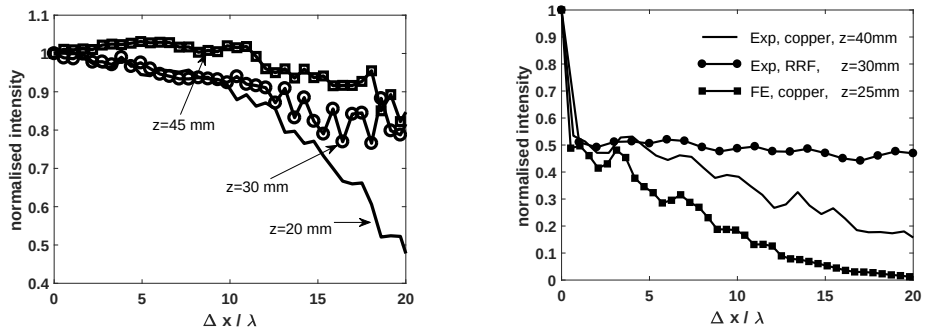

(a) (b)

Fig. 2. The backscattering intensity of the FMC array data in (a) single scattering, and (b) multiple scattering regimes. All intensities correspond to the frequency $f = 5$MHz and the single realisation of random media.

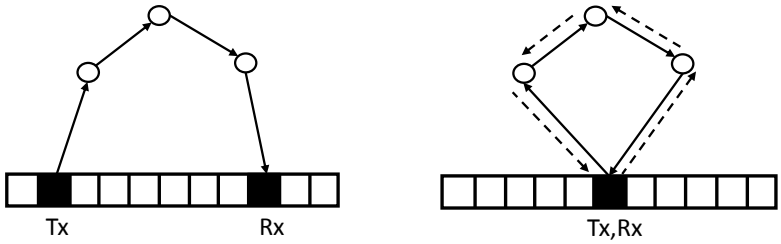

(a) (b)

Fig. 3. Schematic diagram of the multiple scattering paths corresponding to the backscattering intensity $I(\Delta x)$. (a) Different transmitter and receiver elements ($\Delta x \neq 0$); (b) pulse-echo signal ($\Delta x = 0$), reciprocal path is shown as a dash line.

allows for a treatment of an array image as an equivalent "imaging" representation of the original transmitter-receiver array data.

In this paper the back-propagation imaging method is used. The method is represented by a linear operator, B, which converts FMC data, $g_{fmc}(t, x_T, x_R)$, into the generalised image, $b(z, x_T, x_R)$ [23],

$$b(z, x_T, x_R) = B[g_{fmc}(t, x_T, x_R)],\ B = F^{-1}HF. \quad (13)$$

Here F is a two-dimensional Fourier transform with respect to the spatial coordinates x_T, x_R, F^{-1} is the inverse Fourier transform. H is the back-propagation of angular spectrum operator and can be written in the form of a one-dimensional Fourier transform (see Appendix A). The generalized image can be considered as a different representation of the original FMC dataset as they can be transformed between the two representations using the back-propagation and inverse back-propagation, $B^{-1} = F^{-1}H^{-1}F$, operators.

The physical meaning of the generalised image, $b(z, x_T, x_R)$, is transmitter-receiver array data, measured at time $t = 0$ by an array located at depth z [23], [25], [26]. However, in the context of the present paper it is more useful to interpret $b(z, x_T, x_R)$ as a beamforming image with the different transmit, (x_T, z), and receive, (x_R, z), focusing points. Then the conventional two-dimensional image of a scatterer position, $b_{2D}(x, z)$, is given by the pulse-echo part of the generalised image at $x_T = x_R$ plane:

$$b_{2D}(x, z) = b(z, x, x). \quad (14)$$

The next step is to analyse the structure of the single and multiple scattering in the generalised imaging domain. Figs. 4(a), 4(b) and 4(c) show the conventional two-dimensional back-propagation image and the corresponding generalised three-dimensional image for the modelling example of the random single scattering medium. It can be seen that the back-propagation operator focuses the backscattered signals from each scatterer into the vicinity of its location, and, therefore, the data in the generalized image domain are localized around the pulse-echo plane $x_T = x_R$. This reveals the fundamental sparse nature of the single-scattering FMC dataset, which is not observable from the conventional 2D image [24]. Therefore, the generalised image $b(z, x_T, x_R)$ contains more information than is necessary for localization of the scatterers. However, this extra information corresponding to the non-diagonal data $x_T \neq x_R$ is crucial for quantifying the relative amount of single and multiple scattering contributions.

For comparison, Figs. 4(d), 4(e) and 4(f) show the conventional 2D image and the generalised image for the copper sample, when the multiple scattering dominates. It can be seen that 2D images in Figs. 4(a) and 4(d) don't provide enough information in order to distinguish between single and multiple scattering regimes (apart

from the greater attenuation of the image intensity with respect to depth noticeable in Fig. 4(d)). However, this difference becomes apparent when 3D generalised images are considered. We can see that in the multiple scattering case the image intensity is not localised around the pulse-echo plane and is spread over the whole generalised image domain. Note, that a similar effect was recently experimentally observed in optical imaging through a strongly scattering layer [27].

B. Backscattering image intensity

In order to reveal the signatures of single and multiple scattering in the generalised imaging domain, the following processing of the array data is performed. Firstly, the frequency filter is applied to the FMC data in order to obtain narrow frequency band data $g_{fmc}(f,t,x_T,x_R)$, which is then converted into the corresponding generalised images $b(f,z,x_T,x_R) = B[g_{fmc}(f,t,x_T,x_R)]$. In this paper, a Gaussian filter with the centre frequency f and a half bandwidth $0.5f$ is chosen. This ensures that the resolution in the z-direction in terms of wavelengths is the same at all frequencies. Then, by direct analogy to the FMC data analysis, the mean intensity of the generalised image as a function of the distance between transmitter and receiver focussing points, $\Delta x = x_T - x_R$, is considered,

$$I(\Delta x, z, f) = \left\langle |b(f, z', x_T, x_R)|^2 \right\rangle_{|x_T - x_R| = \Delta x, |z' - z| \le \Delta z/2}, \tag{15}$$

where the generalised image b is initially Hilbert transformed with respect to z. Note that the averaging is also performed over depth z and the averaging interval $\Delta z = \alpha_z \lambda$, where α_z is the frequency independent constant. In all examples below $\alpha_z = 5$ was taken.

The single scattering image intensity $I(\Delta x)$ is shown in Fig. 5(a). In this case, the intensity rapidly decays as Δx increases and its behaviour is determined by the Point Spread function (PSF) of the array in the generalised imaging domain. The analytical expression for the asymptotic of the PSF has been derived in [24]. Based on this result, the single scattering intensity in the far-field from the pulse-echo plane $\Delta x/\lambda > 1$ for a random scattering medium can be written as (the full derivation is given in Appendix B)

$$I_S(\Delta x) = a_S I_{Sn}(\Delta x), \quad I_{Sn} = 1.5 \left(2\pi \varphi_0 \frac{\Delta x}{\lambda} \right)^{-2}, \tag{16}$$

where $a_S = \max I_S = I_S(0)$ is the maximum intensity of the conventional 2D image, and the angle φ_0 corresponds to the half angular aperture of the array (see Fig. 1(b)).

Now the situation when the multiple scattering dominates is considered. The corresponding image intensities for different random media are shown in Fig. 5(b). It can be seen that the intensity has a maximum at the pulse-echo plane $\Delta x = 0$. The finite width, $\Delta x \sim \lambda$, of the maximum peak is due to the diffraction limited lateral resolution of the array. At large $\Delta x \gg \lambda$ intensity monotonically decreases due to the array element directivity. However, the most important feature is that outside of the maximum peak, the intensity falls approximately to the half of its maximum value. The physical interpretation of this phenomenon is similar to the coherent backscattering effect for the FMC data and is given below.

The generalised image intensity at the point (x_1, x_2, z) is determined by the scattering paths with the total transmitter-receiver travel distance equals to the sum of the direct paths $(T \to S_{10}) + (S_{20} \to R)$ from the transmitter T to the focusing point $S_{10} = (x_1, z)$ and from the receiver R to the focusing point $S_{20} = (x_2, z)$. For the relatively small incident/scattered angles these scattering paths are represented by $A_p = \{S_1 \to S_2\}$, with the first scatterer at $S_1 = (x_1, z_1)$, the last scatterer at $S_2 = (x_2, z_2)$, and the scattering path length between the first and the last scatterer approximately equals to $(z - z_1) + (z - z_2)$. The schematic diagram is shown in Fig. 6(a). Then, similar to (4), the image intensity can be written as a sum of incoherent and coherent intensities,

$$I = \sum_p |B[A_p]|^2 + \sum_p \sum_{q \ne p} B[A_p] B[A_q]^* = I_{inc} + I_{coh}, \tag{17}$$

where $B[A_p]$ is the generalised image corresponding to the FMC array data associated with the scattering path A_p. If $x_1 \ne x_2$, then all paths, and the corresponding image values $B[A_p]$, are uncorrelated, and the coherent intensity I_{coh} tends to zero. However, if the focusing point is in the pulse-echo plane (corresponding to the conventional 2D image), $x_1 = x_2 = x$, then for each scattering path $A_p = \{(x, z_1) \to (x, z_2)\}$ there is a reciprocal path $A_q = \{(x, z_2) \to (x, z_1)\}$ (see Fig. 6(b)). Both paths A_p and A_q contribute to one imaging point, (x, x, z), and the image values for them are exactly the same, $B[A_p](x, x, z) = B[A_q](x, x, z)$. In this case the coherent intensity is equal to the incoherent intensity, and, therefore, the total intensity is doubled.

C. Multiple scattering estimator in the imaging domain

Now in order to estimate the single and multiple scattering rates the same procedure as in the previous section can be used. The result is represented by expression (10), where averaging over Δx is performed in the area outside of the maximum intensity peak. For all examples in the following sections the averaging interval $3\lambda \le \Delta x \le 8\lambda$ was used. In this case, the normalised multiple scattering intensity $I_{Mn} \approx 0.5$, and the normalised single scattering intensity is given by asymptotic expression (16). Finally, it should be noted, that maximums of the single and multiple scattering intensities are reached at $\Delta x = 0$, or on the pulse-echo plane of the generalised image. Therefore, the estimated single and multiple scattering rates (defined by expression (9)) correspond to the 2D conventional image.

V. Results

In this section, the method for multiple scattering estimation described in the previous section is tested

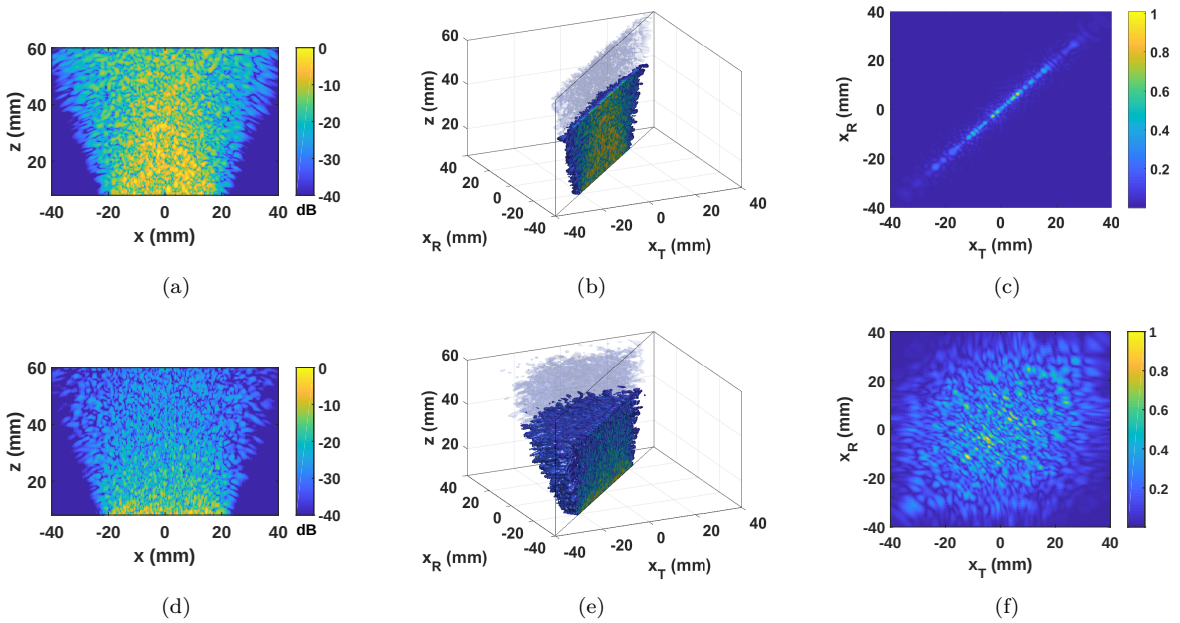

Fig. 4. Imaging results for the copper sample obtained from the single scattering model (a-c), and the experimental measurements (d-f). (a) and (d) 2D conventional image. (b) and (e) Generalised image (isosurfaces at -30dB level, the image is shown for $x_T \leq x_R$, 2D image corresponds to the pulse-echo plane $x_T = x_R$). (c) and (f) Slice of the generalised image at $z = 40$mm. The frequency is 5MHz and the angular filter of 30° is applied to the FMC data.

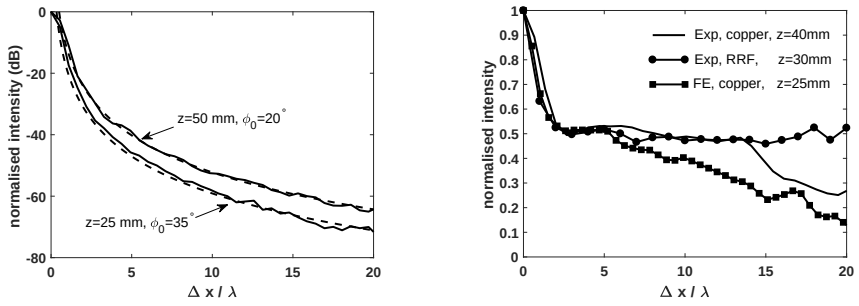

Fig. 5. The generalised image intensity in (a) single scattering (dash line corresponds to theoretical prediction (16) and the angle φ_0 is the angular array aperture at the depth z) and (b) multiple scattering regimes. All intensities correspond to the frequency $f = 5$MHz and the single realisation of random media.

on different random scattering samples. In all cases the angular filter of 25° was applied to the FMC data in the wavenumber domain. It helps to suppress aliasing artifacts related to the array elements under-sampling and edge effects, but has relatively small effect on the image resolution [28] and on the multiple scattering rate estimation.

A. Random Rod Forest sample

First, the RRF specimen is considered as the example of a random scattering medium. In this case the FMC data were measured using the 5MHz 128 elements array #2. The time window $\Delta t = 5$ μs was taken in the Short-time Fourier transform for the multiple scattering estimation in the time domain. Additionally, the Gaussian frequency filter with the center frequency f and a half bandwidth $0.5f$ was applied to the FMC data $G_{fmc}(T, f', x_T, x_R)$ before averaging in expression (3), in order to be consistent with the multiple scattering estimation in the imaging domain.

Results of data processing steps are shown in Fig. 7. Fig. 7(a) shows the conventional 2D image. The multiple scattering rate as a function of frequency and depth estimated from the FMC and generalised image data is shown in Fig. 7(b) and 7(c), respectively. It can be seen from Fig. 7(b) that the multiple scattering dominates in the FMC data at all frequencies and depths considered with the rate from 80% to 100%. On the other hand, as has been discussed in the previous section, the image is much more sensitive to the single scattering compared with the raw data. In this case, as Fig. 7(c) demonstrates, the sharp transition region at the depth of approximately 10-15 mm

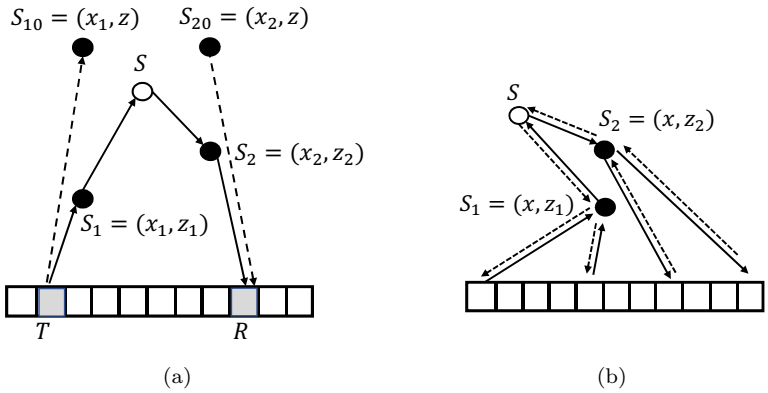

(a) (b)

Fig. 6. Schematic diagram of the multiple scattering paths corresponding to the generalised image intensity $I(\Delta x)$. S_1 is the first scatterer, S_2 is the last scatterer and S is the intermediate scatterer involved in the scattering path between S_1 and S_2. (a) Different transmitter (S_{10}) and receiver (S_{20}) focussing points ($\Delta x \neq 0$). Scattering path $T \to S_1 \to S \to S_2 \to R$ equals to the sum of the direct paths $(T \to S_{10}) + (S_{20} \to R)$ from the transmitter T to the focusing point S_{10} and from the receiver R to the focusing point S_{20}; (b) pulse-echo focussing point ($\Delta x = 0$), reciprocal path is shown as a dash line.

is clearly identified, when the multiple scattering rate rapidly increases from 50% to 100%. On the contrary, this transition is barely seen in Fig. 7(b), highlighting the superiority of the image based multiple scattering rate estimation method. Therefore, for all examples below only the method of multiple scattering rate estimation from the generalised image is considered.

Note that the RRF has a relatively sparse distribution of scatterers compared to the ultrasonic wavelength. As a result, in the dominant single scattering regime the scatterers are individually resolvable on the conventional 2D image. At the same time, the multiple scattering manifests itself as a background noise and in the dominant multiple scattering regime the image represents a speckle pattern without connection to the individual scatterers. Therefore, in this particular case the transition from single to multiple scattering becomes visible on the conventional image as it is seen in Fig. 7(a). These qualitative observations can be quantified by the following metric

$$\delta_I(z, f) = \frac{\left\langle |b_{2D}|^2 \right\rangle_x}{\max\limits_x |b_{2D}|^2}. \tag{18}$$

In the pure single scattering case $\delta_I \sim \rho_S A_S \ll 1$, where ρ_S is the density of scatterers and A_S is the image area of one scatterer. When the multiple scattering contribution increases, δ_I also increases . The metric (18) is shown in Fig. 7(d) as a function of frequency and image depth. It can be seen that the transition between single and multiple scattering regimes is in a good agreement with Fig. 7(c). The discrepancy between two estimations at the frequencies $f > 3$ MHz in the transition region $z \approx 15$ mm is explained by the fact that the generalised image method is based on the averaged image properties. For the RRF sample the average single scattering intensity is always smaller (and, therefore, estimated multiple scattering rate is higher), compared to metric (18), where the maximum image amplitude is used.

It needs to be stressed that the multiple scattering estimation method (10) is based entirely on the generalised image values outside of its main diagonal plane $x_T = x_R$, corresponding to the conventional 2D image. Therefore, the method is also applicable to a random scattering medium with the distance between scatterers smaller than the ultrasonic wavelength (for example, grains in polycrystalline metals), when the corresponding 2D image displays only a speckle pattern at all depths (see Figs. 4(a), 4(d)).

B. Copper sample

Next, the measurements were conducted on a 100 mm deep copper sample using the 5 MHz 128 elements array #2. The first group of measurements was taken on the defect free part of the sample at 10 different locations. The multiple scattering rate as a function of frequency and depth was estimated from each of the FMC data sets and then averaged over all measurements. The final result is shown in Fig. 8(a). The transition between dominant single (at small depths and low frequencies) and dominant multiple scattering (at large depths and high frequencies) regions is clearly visible. It can be seen that the multiple scattering rate strongly depends on both frequency and depth and increases very quickly from around 40% till 100% in the transition region.

The variability of the multiple scattering rate estimated using different measurements is shown in Fig. 8(b). It can be seen that in the dominant single scattering regime the standard deviation is generally small, and varies from 5% to 10%. When the multiple scattering increases, the standard deviation also increases, and this changes between 10% and 20%.

One application of the proposed method is a possibility to provide a quantitative assessment of the defect detection in coarse grain materials. The defect's detectability is usually characterised by the signal-to-noise ratio, δ_{SNR}. The signal here represents the maximum image amplitude of the defect, and the appropriate noise measure is the root

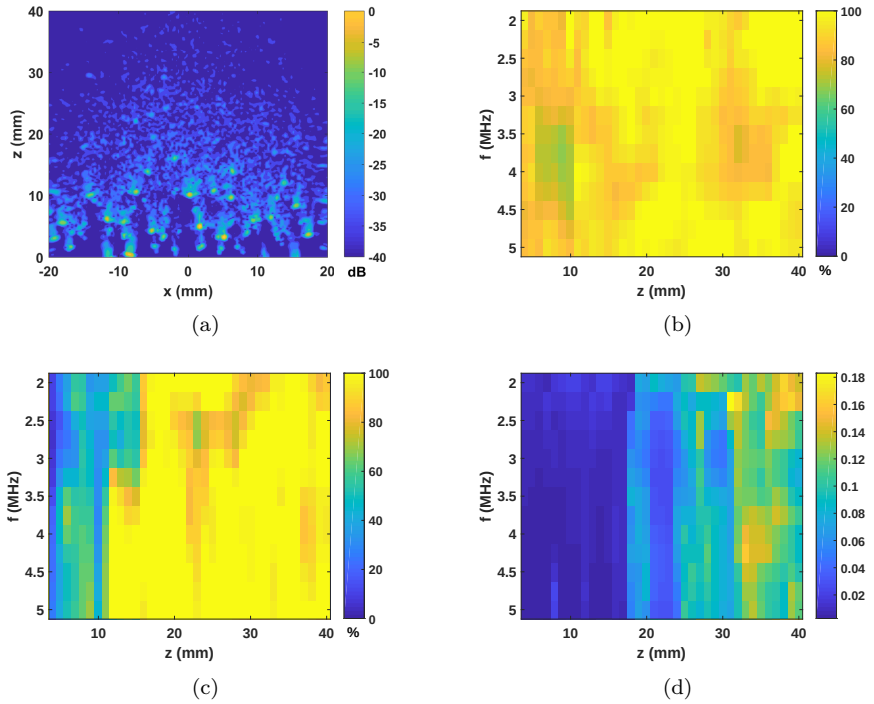

Fig. 7. Experimental results for the RRF sample using 5 MHz 128 elements array. (a) Back-propagation image at 3 MHz, $z = 0$ corresponds to the front edge of the sample. (b) Multiple scattering rate in the FMC data. For convenience the time T is converted into the depth as $z = Tc/2$, where $c = 1500$ m/s is speed of sound in water. (c) Multiple scattering rate in the image. (d) Metric δ_I calculated using expression (18).

mean square (RMS) of the grain noise image amplitude. Then δ_{SNR} can be written as

$$\delta_{SNR}(z_d, f) = \frac{\max|b_{2D}|}{\sqrt{\langle|b_{2D}|^2\rangle}}, \tag{19}$$

where the maximum is taken in the vicinity of the defect location (x_d, z_d). The grain noise averaging is performed outside the defect location and at the same depth to the defect, $|z - z_d| \leq \Delta z/2$. In the examples below, Δz was chosen similar to the multiple scattering rate estimation, $\Delta z = 5\lambda$ (see expression (15)).

A detection threshold is needed to determine the existence of a defect. It is assumed that the grain noise image amplitude follows a Rayleigh distribution [29]. If there are N independent pixels in the considered image area, then the probability of false alarm, p_{fa}, is given by

$$p_{fa} = 1 - \left(1 - e^{-\delta^2_{SNR}}\right)^N. \tag{20}$$

If $p_{fa} \ll 1$, then the required threshold can be estimated as

$$\delta_{SNR} = \sqrt{\ln \frac{N}{p_{fa}}}. \tag{21}$$

In the examples below $N \sim 100$ and the false alarm rate is set to $p_{fa} = 1/1000$, therefore the detection threshold is 3.4 or 10.6 dB.

The second set of FMC array data was collected for 2 mm diameter side-drilled holes located at the depths 19 mm, 29 mm, 40 mm and 57 mm directly below the array center. The SNR was estimated at the frequencies between 2 MHz to 7 MHz. The images at different frequencies for the defect located at 40 mm depth are shown in Fig. 9. It can be seen that at 2.5 MHz (the multiple scattering rate is about 50%) the noise is relatively small compared to the defect image amplitude and $\delta_{SNR} = 32$ or 30 dB (Fig. 9(a)). Then the SNR rapidly decreases with frequency and at 3.5 MHz (the multiple scattering rate is about 80%) drops to approximately $\delta_{SNR} = 10$ or 20 dB (Fig. 9(b)). Finally, in the dominant multiple scattering regime at 4.7 MHz (the multiple scattering rate is around 100%) the SNR reaches the detection threshold of 3.4 and the image amplitude of the defect becomes comparable with the maximum grain noise image amplitude (Fig. 9(c)).

The images in Fig. 9 show that the detection limit is closely correlated with the onset of the dominant multiple scattering regime, when the single scattering rate becomes negligibly small. This fact is further illustrated in Fig. 10, where the SNR is shown alongside the single scattering rate. The thresholds (0% for the single scattering rate and 3.4 for the SNR) are also plotted as a dotted line. For the defect located at $z = 19$ mm, the SNR remains above the detection threshold in the considered frequency range. This behaviour agrees with the corresponding single scattering rate, which is around 10% even at 7 MHz. However, it can be seen that for the three other deeper defects the detection limit is reached shortly after the

single scattering rate becomes close to zero. This is also shown in Fig. 8(a), where the black circles indicate the threshold detection frequencies corresponding to the defects at different depths.

Note that the negative values of the single scattering rate in Fig. 10 are nonphysical. This situation might occur in the dominant multiple scattering regime, when the measured signals are small due to attenuation and affected by the random noise. Expression (10) for the single and multiple scattering rates is based on the assumption that the generalised image intensity outside of the main diagonal plane (corresponding to the 2D image) equals exactly to the half of its maximum value in the dominant multiple scattering regime. However, in reality the intensity fluctuate around half of its maximum value and can slightly exceed it, making the multiple scattering rate greater than 100%.

C. Finite Element model

In this section the proposed multiple scattering estimation method is applied to the FMC array data generated using the FE model [14]. In order to perform statistical analysis 30 random grain structures were simulated. The FMC data were modeled for the 2.5 MHz 64 elements array #1. A wideband input signal, formed of a single cycle toneburst, was used for all the simulations to allow for a single model run to provide results for a wide range of frequencies.

The estimated multiple scattering rate as a function of frequency and depth, averaged over 30 realisations, is shown in Fig. 11(a). The transition from single to dominant multiple scattering regime is clearly observable between 2.5 and 3.5 MHz in the considered depth range from 15 mm to 30 mm. The standard deviation is also shown in Fig. 11(b). The lowest variability (from 5% to 10%) is in the predominantly single scattering zone at frequencies less than 3MHz. In the dominant multiple scattering regime at frequencies greater than 5MHz the standard deviation is slightly higher and is between 10% and 15%. The maximum standard deviation of 20% corresponds to the onset of the dominant multiple scattering at frequencies from 3MHz to 5MHz.

A crack of 2mm length and holes of sizes 0.5mm and 2mm located at depth $z = 21$mm are chosen as target defects, and the random grain structures are used to simulate array data for these defects. The images for the 2mm crack at different frequencies are shown in Fig. 12. It can be seen in Fig. 12(a) that the defect is reliably detectable in the predominantly single scattering regime at 2.5MHz ($\delta_{SNR} = 35$ or 31dB and multiple scattering rate is 37%). Then the SNR starts to rapidly decrease in the transition region between single and multiple scattering, for example at 4MHz the multiple scattering rate increases to 95% and the SNR decreases to $\delta_{SNR} = 7$ or 17dB (Fig. 12(b)). In the dominant multiple scattering regime at 5.5MHz the defect becomes almost non-detectable with $\delta_{SNR} = 3.5$, which is very close to the threshold of 3.4 (Fig. 12(c)).

The SNR for all defects as a function of frequency is shown in Fig. 13 together with the single scattering rate at the depth $z = 21$mm, corresponding to the location of the defects. The dotted line represents the threshold (0 dB for the single scattering rate and 3.4 for the SNR). This graph shows that similar to the previous case the imaging performance for all defects is strongly correlated with the onset of the dominant multiple scattering. This is also shown in Fig. 11(a), where the black circles indicate the threshold detection frequencies for different defects.

D. Discussion

All cases considered above show that the behaviour of the SNR as a function of frequency is directly correlated with the single scattering rate at the same depth. Moreover, it is possible to distinguish between two different regimes (in the considered frequency range). First, the SNR rapidly decreases with frequency until the single scattering rate becomes close to zero, which corresponds to the onset of the dominant multiple scattering. Note, that a drop in the performance is significant and is approximately 1-2 orders of magnitude higher compared to the maximum SNR at low frequencies. After that the SNR continues to decrease until it reaches the detection threshold, but at a much slower rate.

The obtained results have an important practical implication. It is known that the decrease in the imaging performance in random scattering media at high frequencies and large depths results from two different physical phenomena, scattering and absorption [6]. In polycrystalline materials, at frequencies typically used in NDT (below 20 MHz), the absorption is negligibly small [30], so the underlying physical reason of poor detection is the increased multiple scattering. However, quantitative estimates of the detection limit are usually obtained for specific defects by numerical modeling [14] or experimental measurements [4], [31] and without direct relation to the multiple scattering rate.

The examples in this section provide evidence that the critical frequencies and depths at which defects become undetectable can be estimated from the backscattering array data only. Moreover, the method doesn't require any prior knowledge about the material microstructure (for example, grain size) or any additional modeling/measurements to be undertaken. The method is based entirely on the properties of the single and multiple scattering in the generalised imaging domain, and, therefore, can be applied to any random scattering medium.

The final comment is related to the backpropagation imaging method. It was shown that the backpropagation method and other well known linear imaging methods, including the Total Focusing method (TFM), the wavenumber algorithm, Inverse Wave-field Extrapolation and the plane wave imaging method [24], [32], are closely related to each other and can all be expressed in the delay and sum form. It means that all results obtained here are also directly applicable to these imaging algorithms as well.

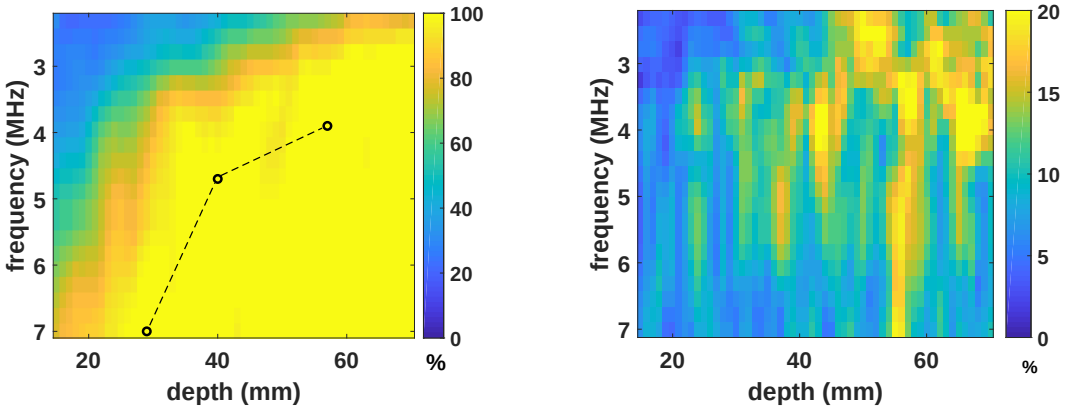

(a) (b)

Fig. 8. Experimental results for the copper sample using 5 MHz 128 elements array. (a) Multiple scattering rate in the image averaged over 10 measurements. Black circles correspond to the detection limit of 2mm holes located at 29mm, 40mm and 57mm depths. Linear interpolation (dotted line) is used in order to indicate the area (above the curve) in the frequency-depth space where detection is possible. (b) Standard deviation of the estimated multiple scattering rate.

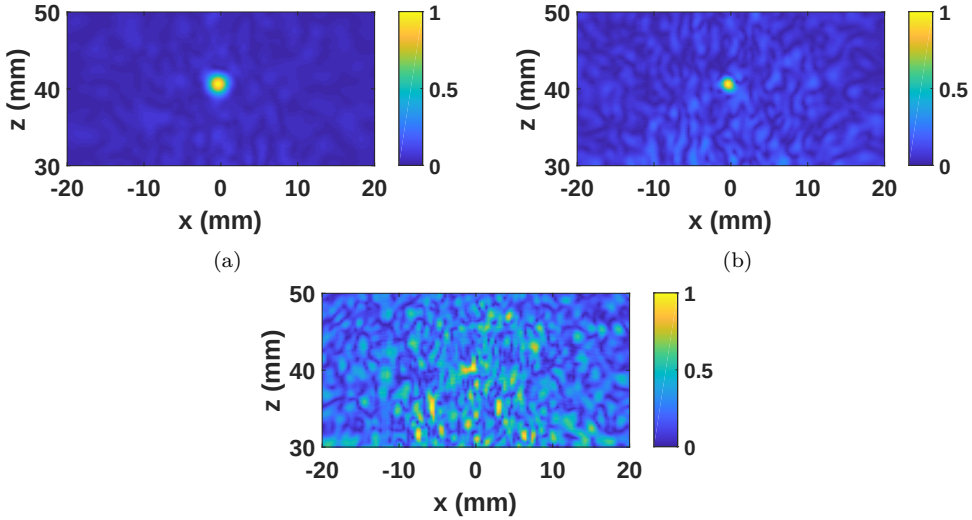

(a) (b)

(c)

Fig. 9. Images of 2mm hole located at 40mm depth in the copper sample obtained using 5MHz 128 elements array at frequencies of (a) 2.5MHz, (b) 3.5MHz and (c) 4.7MHz.

It should be noted that the proposed method is based on the assumption that the background material velocity is known, so it is possible to apply the imaging procedure. In all examples here scattering media are purely random, and the velocity distribution can be considered as isotropic and homogeneous. However, in some applications, for example, exploration seismology, a propagation medium is often anisotropic and inhomogeneous, and an accurate estimation of the background velocity can be challenging.

VI. Conclusion

A method for estimating the multiple scattering proportion in a random scattering medium has been developed. The backscattering transmitter-receiver data are measured using a linear transducer array. The method doesn't need to physically separate single and multiple scattering contributions, and is based on the specific behaviour of the backscattering intensity in the single and multiple scattering regimes.

It has been shown that the sensitivity of the time-domain method to the single scattering is relatively low and the accuracy is limited because of the near-field measurement configuration. These limitations can be alleviated if the array data is considered in the generalised imaging domain, which represents an image with different focusing points on transmission and reception. In this case, the multiple scattering contribution is spread over the whole generalised imaging domain, and exhibit a specific structure similar to the coherent backscattering phenomenon. On the contrary, the single scattering contribution is focused in the vicinity of the pulse-echo plane, corresponding to the conventional 2D image. The focusing

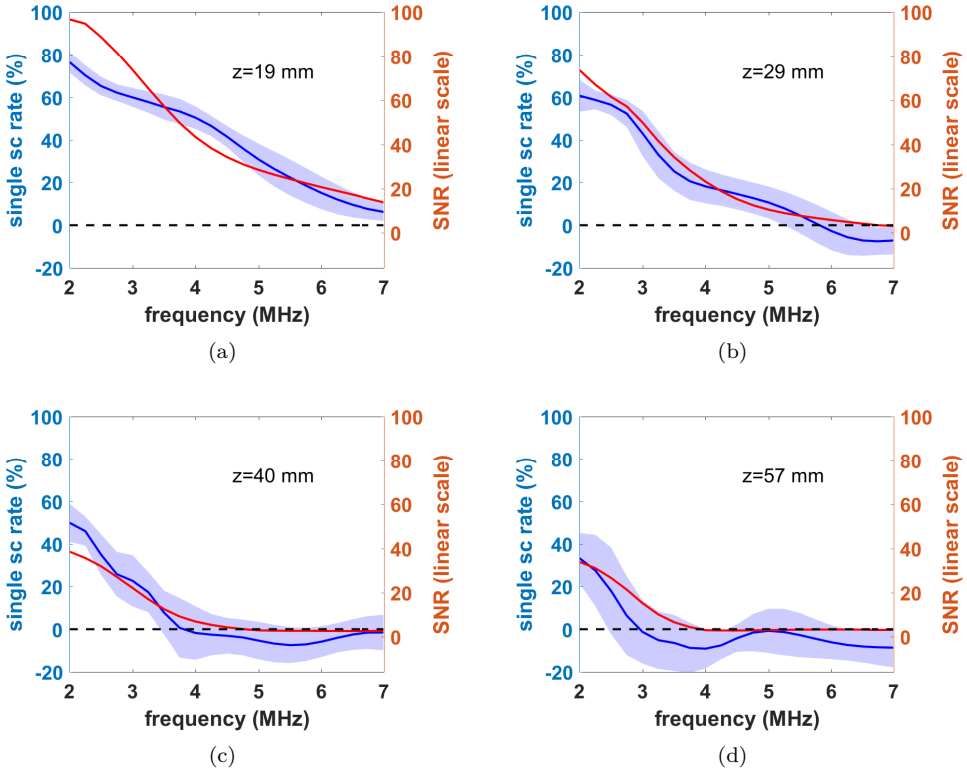

Fig. 10. SNR as a function of frequency (red line) for 2mm holes located at (a) 19mm, (b) 29mm, (c) 40mm and (d) 57mm depths in the copper sample. The corresponding mean single scattering rate is shown as a blue line, with the shaded region representing one standard deviation. Dotted line designates a threshold of 0% for the single scattering rate and 3.4 (10.6dB) for the SNR.

effect provides at least one order of magnitude improvement in sensitivity to the single scattering contribution compared to the time-domain approach. Moreover, it has been demonstrated on the experimental and simulated data, that the achieved sensitivity is high enough to capture the transition from dominant single to dominant multiple scattering on the array image.

The developed method can be used to experimentally validate the single scattering model (the first Born approximation), which is a common tool to study imaging in a random scattering medium. Another important practical application is to provide a quantitative assessment and optimisation of the array imaging performance in highly scattering materials. In particular, it has been shown that the signal-to-noise ratio (SNR) as a function of frequency and imaging depth is directly correlated with the estimated single scattering rate. Moreover, the detection limit corresponds to the onset of the dominant multiple scattering regime, when the multiple scattering rate approaches 100%. Additionally, the multiple scattering rate as a function of depth and frequency is sensitive to material microstructure and potentially can also be used for material characterisation. Finally, the proposed method can be applied to other types of waves and areas where transmitter-receiver arrays are used for imaging and detection (e.g. underwater acoustics, seismology, radar, sonar, etc.).

Appendix A
Back-propagation of angular spectrum operator

In this section, the expression for the back-propagation of the angular spectrum operator H is given. Any time-domain signal $u(t)$ can be expressed as a linear superposition of its spectral components $u(\omega)$,

$$u(t) = \frac{1}{2\pi}\int u(\omega)e^{i\omega t}d\omega. \tag{22}$$

The Fourier transform operator F transforms the FMC array data $g_{fmc}(t, x_T, x_R)$ into the angular spectrum $G(t, k_{x(T)}, k_{x(R)})$, where $k_{x(T)}$ and $k_{x(R)}$ are the wavenumbers in the x-direction for the transmitted and scattered waves, respectively:

$$G(t, k_{x(T)}, k_{x(R)}) \equiv F[g_{fmc}(t, x_T, x_R)] = \int\int g_{fmc}(t, x_T, x_R)\, e^{i(k_{x(T)}x_T + k_{x(R)}x_R)}\, dx_T dx_R. \tag{23}$$

Note, that the back-propagation operation is based on the assumption that the transmitter and receiver elements are sensitive to the longitudinal wave mode only. Then it can be shown [23] that the angular spectrum, $G(t, k_{x(T)}, k_{x(R)})$, represents a 1D wave propagating in the z direction with the wavenumber $k_z = k_{z(T)} + k_{z(R)}$. Here $k_{z(T)} = \sqrt{k^2 - k_{x(T)}^2}$, $k_{z(R)} = \sqrt{k^2 - k_{x(R)}^2}$ are the wavenumbers in the z-direction for the transmitted and scattered wave, and $k = \omega/v$ is the scalar wavenumber,

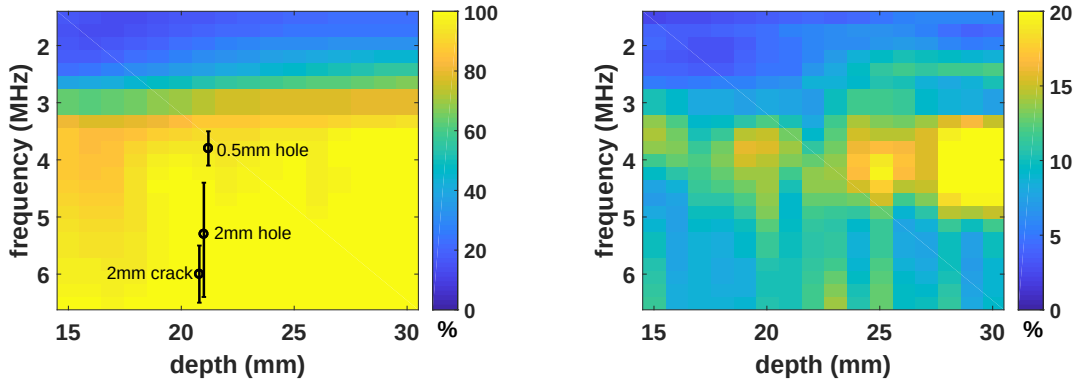

(a) (b)

Fig. 11. FE results for the copper sample with 0.1mm mean grain size using 2.5 MHz 64 elements array. (a) Multiple scattering rate in the image averaged over 30 random grain structures. Black circles correspond to the detection limit of different defects with error bars representing one standard deviation. (b) Standard deviation of the estimated multiple scattering rate.

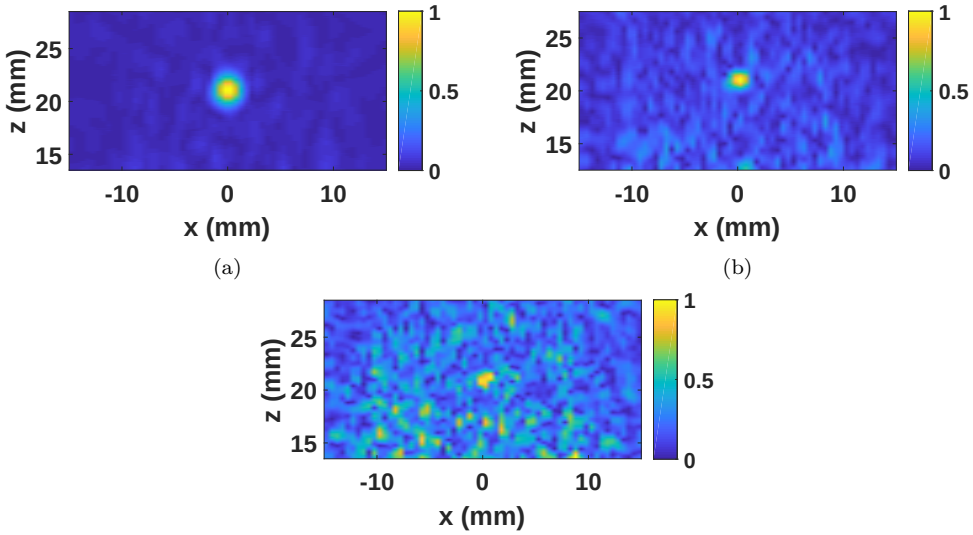

(a) (b) (c)

Fig. 12. Images of 2mm crack located at 21mm depth in the copper sample with 0.1mm mean grain size obtained using 2.5 MHz 64 elements array (FE simulations) at frequencies of (a) 2.5MHz, (b) 4MHz and (c) 5.5MHz.

where v is the velocity of the longitudinal wave. The back-propagation of the angular spectrum operator H converts the time data $G(t, k_{x(T)}, k_{x(R)})$ into a function of propagation distance, $h(z, k_{x(T)}, k_{x(R)})$, and can be written in the form:

$$h(z, k_{x(T)}, k_{x(R)}) \equiv H[G(t, k_{x(T)}, k_{x(R)})] = \frac{1}{2\pi} \int G(\omega, k_{x(T)}, k_{x(R)})\, e^{ik_z z}\, d\omega. \tag{24}$$

For the spatial wavenumbers $k_{x(T)}, k_{x(R)} > k$ the spectrum $G(\omega, k_{x(T)}, k_{x(R)})$ corresponds to the exponentially decaying evanescent waves and it can be assumed that $G(\omega, k_{x(T)}, k_{x(R)}) = 0$ for $k_{x(T)}, k_{x(R)} > k$. The wavenumber k_z non-linearly depends on the frequency ω and its direct calculation using the formula (24) is very time consuming. However, if the integration variable is changed from ω to k_z then the integral (24) can be written in the form of a Fourier transform with respect to the variable k_z as

$$h(z, k_{x(T)}, k_{x(R)}) = \frac{1}{2\pi} \int G(\omega(k_z), k_{x(T)}, k_{x(R)}) \times \left(\frac{dk_z}{d\omega}\right)^{-1} e^{ik_z z}\, dk_z. \tag{25}$$

Appendix B
Single scattering intensity in the generalised imaging domain

In this section the derivation of expression (16) for the single scattering intensity in the generalised image domain as a function of transmitter-receiver distance, Δx, is given.

The analysis is based on the analytical expression for the Point Spread function (PSF) in the generalised image domain [24]. The location of the scatterer is denoted by

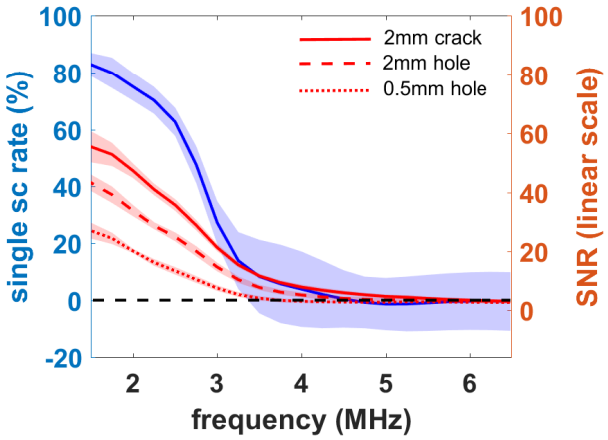

Fig. 13. SNR as a function of frequency (red line) for 2mm crack, 2mm hole and 0.5mm hole, located at 21mm depth in the copper sample with 0.1mm mean grain size (FE simulations). The corresponding mean single scattering rate is shown as a blue line, with the shaded region representing one standard deviation. Dotted line designates a threshold of 0% for the single scattering rate and 3.4 (10.6dB) for the SNR.

(x_0, z_0). It was shown that the side lobes of the PSF are located in the (x_T, z), (x_R, z) planes and their direction is defined by the angle $\theta = \theta_P$:

$$\theta_P = \frac{\pi}{2} \mp \frac{\varphi_0}{2}, \tag{26}$$

where the angle θ is an elevation angle in the $(x_T - x_0, x_R - x_0, z - z_0)$ space, and $\theta = 0$ corresponds to the direction of the positive z-axis. The angle φ_0 corresponds to the maximum scattered angle measured by the array (half angular aperture of the array, see Fig. 1(b)).

The behaviour of the PSF depends on the angular aperture of the array φ_0. For the measurement configurations considered in this paper the asymptotic expression for the relative side lobe level is given by [24]:

$$\delta_P(\tilde{r}, \varphi_0) = \frac{1}{4\pi\tilde{r}} \frac{1}{\varphi_0 \cos\frac{\varphi_0}{2}} \tag{27}$$

where $\tilde{r} = r/\lambda$ and r is the radial distance in the $(x_T - x_0, x_R - x_0, z - z_0)$ space with the centre at the location of the scatterer.

In a random medium composed of randomly distributed point scatterers, the generalised image amplitude at the point (x_T, x_R, z) is given by the superposition of the side lobes of four scatterers located at $\mathbf{r}_{1,2} = (x_T, z \pm \delta z)$ and $\mathbf{r}_{3,4} = (x_T + \Delta x, z \pm \delta z)$, where $\delta z = |\Delta x| \tan 0.5\varphi_0$, $\Delta x = x_R - x_T$. This fact follows from the structure of the PSF in the generalised image domain. Then the image intensity can be written in the form

$$I_S(\Delta x) = a_S I_{Sn}(\Delta x), \quad I_{Sn}(\Delta x) = 4\alpha_P \delta_P^2, \tag{28}$$

where $a_S = \max_{\Delta x} I_S = I_S(0)$ is the intensity of the conventional 2D image. The coefficient α_P depends on the correlation coefficients, ρ_{ij}, between image values at the locations $\mathbf{r}_i$, $\mathbf{r}_j$ and is given by

$$\alpha_P = 1 + \frac{1}{4} \sum_{i \neq j} \rho_{ij}. \tag{29}$$

If all scatterers are uncorrelated, then $\rho_{ij} = 0$ and $\alpha_P = 1$. Note, that the single and multiple scattering rates are estimated using the generalised image intensity at $\Delta x \geq 2\lambda$ (see section IV). Hence, it can be assumed that image values at $\mathbf{r}_{1,2}$ and $\mathbf{r}_{3,4}$ are uncorrelated, $\rho_{13}, \rho_{14}, \rho_{23}, \rho_{24} = 0$. On the other hand, for small angles $\varphi_0 \ll 1$ the values of $\delta z < \lambda$. In this case the image values at $\mathbf{r}_1$ and $\mathbf{r}_2$, and also $\mathbf{r}_3$ and $\mathbf{r}_4$, cannot be considered as totally uncorrelated and $\alpha_P \approx 2$. Therefore, in general $1 \leq \alpha_P \leq 2$.

Finally, the distance r from the locations of the scatterers $\mathbf{r}_i$ to the imaging point is related to the transmitter-receiver distance as

$$r = \frac{|\Delta x|}{\cos\frac{\varphi_0}{2}}. \tag{30}$$

Then expression (16) for the single scattering generalised image intensity $I_{Sn}(\Delta x)$ follows from (27), (28) and (30).

Note, that for all measurement configurations considered in this paper, $\varphi_0 \geq 15°$ and, hence, $I_{Sn} \ll I_{Mn} = 0.5$ for $\Delta x > 1$. Then the variation of α_P between values 1 and 2 results in a relatively small variation of single and multiple scattering rates (defined by expression (10)). Therefore, for simplicity, in all calculations the constant value of $\alpha_P = 1.5$ was chosen. In this case possible inaccuracy in the single and multiple scattering rates is less than 4%.

References

[1] P. D. Wilcox, "Array imaging of noisy materials," AIP Conference Proceedings, vol. 1335, pp. 890–897, 2011.

[2] S. Mahaut, J.-L. Godefroit, O. Roy, G. Cattiaux, "Application of phased array techniques to coarse grain components inspection," Ultrasonics, vol. 42, pp. 791-796, April 2004.

[3] M. Spies, H. Rieder, "Synthetic aperture focusing of ultrasonic inspection data to enhance the probability of detection of defects in strongly attenuating materials," NDT & E International, vol. 43, 5, pp. 425-431, 2010.

[4] J. Zhang, B. W. Drinkwater, P. D. Wilcox, "Comparison of ultrasonic array imaging algorithms for nondestructive evaluation," IEEE Trans. Ultrason. Ferroelectr. Freq. Control vol. 60, no. 8, pp. 1732-1745, 2013.

[5] M. I. Mishchenko, L. D. Travis, A. A. Lacis, "Multiple scattering of light by particles : radiative transfer and coherent backscattering," Cambridge : Cambridge University Press, 2006.

[6] A. Aubry, A. Derode, "Multiple scattering of ultrasound in weakly inhomogeneous media: Application to human soft tissues," J. Acoust. Soc. Am., vol. 129, no. 1, pp. 225-233, 2011.

[7] R. S. Wu, "Multiple scattering and energy transfer of seismic waves - separation of scattering effect from intrinsic attenuation - I. Theoretical modelling," Geophysical Journal International, vol. 82, no. 1, pp. 57–80, 1985.

[8] J. M. Bordier, M. Fink, A. le Brun, and F. Cohen-Tenoudji, "The influence of multiple scattering in incoherent ultrasonic inspection of coarse grain stainless steel," in Proceedings of the IEEE 1991 Ultrasonics Symposium, vol. 2, pp. 803–808, 1991.

[9] M. A. H. Zuberi, T. Alkhalifah, "Generalized Internal Multiple Imaging," Geophysics, vol. 79, no. 5, pp. S207–S216, 2014.

[10] C. Annis, L. Gandossi, and O. Martin, "Optimal sample size for probability of detection curves," Nuclear Engineering and Design, vol. 262, pp. 98–105, 2013.

[11] P. Huthwaite, "Accelerated finite element elastodynamic simulations using the GPU," J. Comput. Phys., vol. 257, pp. 687–707, 2014.

[12] A. Van Pamel, G. Sha, S. I. Rokhlin, M. J. S. Lowe, "Finite-element modelling of elastic wave propagation and scattering within heterogeneous media," Proc. R. Soc. A, 473: 20160738, 2017.

[13] H. A. Bloxham, A. Velichko, and P. D. Wilcox, "Combining simulated and experimental data to simulate ultrasonic array data from defects in materials with high structural noise," IEEE Trans. Ultrason. Ferroelectr. Freq. Control, vol. 63, pp. 2198–2206, December 2016.

[14] H. A. Bloxham, A. Velichko, and P. D. Wilcox, "Establishing the limits of validity of the superposition of experimental and analytical ultrasonic responses for simulating imaging data," IEEE Trans. Ultrason. Ferroelectr. Freq. Control, vol. 66, pp. 101–108, January 2019.

[15] R. B. Thompson, F. J. Margetan, P. Haldipur, L. Yu, A. Li, P. Panetta, H. Wasan, "Scattering of elastic waves in simple and complex polycrystals," Wave Motion, vol. 45, no. 5, pp. 655–674, 2008.

[16] T. Bedetti, V. Dorval, F. Jenson and A. Derode, "Characterisation of ultrasonic structural noise in multiple scattering media using phased arrays," Journal of Physics: Conference Series, vol. 457, 012003, 2013.

[17] A. Aubry, A. Derode, "Detection and imaging in a random medium: A matrix method to overcome multiple scattering and aberration," J. Appl. Phys., 106, 044903, 2009.

[18] S. Shahjahan, F. Rupin, A. Aubry and A. Derode, "Evaluation of a multiple scattering filter to enhance defect detection in heterogeneous media," J. Acoust. Soc. Am., 141 (1), pp. 624–640, 2017.

[19] S. Shahjahan, F. Rupin, A. Aubry, B. Chassignole, T. Fouquet, A. Derode, "Comparison between experimental and 2-D numerical studies of multiple scattering in Inconel600 by means of array probes," Ultrasonics, vol. 54, pp. 358–367, January 2014.

[20] A. Baelde, J. Laurent, P. Millien, R. Coulette, W. B. Khalifa, F. Jenson, F. Sun, M. Fink, C. Prada, "Effect of microstructural elongation on backscattered field: Intensity measurement and multiple scattering estimation with a linear transducer array," Ultrasonics, vol. 82, pp. 379-389, January 2018.

[21] A. Tourin, A. Derode, A. Peyre, M. Fink, "Transport parameters for an ultrasonic pulsed wave propagationg in a multiple scattering medium,", J. Acoust. Soc. Am., 108 (2), pp. 503–512, 2000.

[22] C. Holmes, B. W. Drinkwater, P. D. Wilcox, "Post-processing of the full matrix of ultrasonic transmit-receive array data for non-destructive evaluation," NDT E Int., vol. 38, pp. 701-711, 2005.

[23] A. Velichko, P. D. Wilcox "Reversible back-propagation imaging algorithm for post-processing of ultrasonic array data," IEEE Trans. Ultrason. Ferroelectr. Freq. Control, vol.56, no.11, pp.2492-2503, 2009.

[24] A. Velichko, A. J. Croxford, "Strategies for data acquisition using ultrasonic phased arrays," Proc. R. Soc. A, 474: 20180451, 2018.

[25] N. Pörtzgen, D. Gisolf, and G. Blacquiére, "Inverse wave field extrapolation: A different ndi approach to imaging defects," IEEE Trans. Ultrason. Ferroelectr. Freq. Control, vol.54, no.1, pp.118-127, 2007.

[26] T. Alkhalifah, S. Fomel, and Z. Wu, "Source–receiver two-way wave extrapolation for prestack exploding-reflector modelling and migration," Geophysical prospecting, vol.63, pp.23-34, 2015.

[27] A. Badon, D. Li, G. Lerosey, A. C. Boccara, M. Fink and A. Aubry, "Smart optical coherence tomography for ultra-deep imaging through highly scattering media", Science Advances, vol. 2, no. 11, e1600370, 2016.

[28] P. D. Wilcox and J. Zhang, "Quantification of the Effect of Array Element Pitch on Imaging Performance," IEEE Trans. Ultrason. Ferroelectr. Freq. Control, vol. 65, no. 4, pp. 600-616, 2018.

[29] R. L.T. Bevan, J. Zhang, N. Budyn, A. J. Croxford and P. D. Wilcox, "Experimental quantification of noise in linear ultrasonic imaging", IEEE Trans. Ultrason. Ferroelectr. Freq. Control, vol. 66, pp. 79-90, January 2019.

[30] E. P. Papadakis, "Revised Grain-Scattering Formulas and Tables," J. Acoust. Soc. Am., vol. 37, no. 4, pp. 703–710, 1965.

[31] A. Van Pamel, C. R. Brett, and M. J. S. Lowe, "A Methodology for Evaluating Detection Performance of Ultrasonic Array Imaging Algorithms for Coarse-Grained Materials", IEEE Trans. Ultrason. Ferroelectr. Freq. Control, vol. 61, no. 12, pp.2042-2053, 2014.

[32] A. Velichko, P. D. Wilcox "An analytical comparison of ultrasonic array imaging algorithms," J. Acoust. Soc. Am., vol. 127, no. 4, pp. 2377–2384, 2010. vol.56, no.11, pp.2492-2503, 2009.